Lab on a Chip

PAPER

View Article Online
View Journal | View Issue

Cite this: *Lab Chip*, 2014, **14**, 3341

A light-sheet microscope compatible with mobile devices for label-free intracellular imaging and biosensing†

Tsung-Feng Wu,*[a] Tony Minghung Yen,[b] Yuanyuan Han,[c] Yu-Jui Chiu,[a] Eason Y.-S. Lin[d] and Yu-Hwa Lo[ac]

Received 28th February 2014,
Accepted 20th May 2014

DOI: 10.1039/c4lc00257a

www.rsc.org/loc

The inner structure, especially the nuclear structure, of cells carries valuable information about disease and health conditions of a person. Here we demonstrate a label-free technique to enable direct observations and measurements of the size, shape and morphology of the cell nucleus. With a microfabricated lens and a commercial CMOS imager, we form a scanning light-sheet microscope to produce a dark-field optical scattering image of the cell nucleus that overlays with the bright-field image produced in a separate regime of the same CMOS sensor. We have used the device to detect nuclear features that characterize the life cycle of cells and have used the nucleus volume as a new parameter for cell classification. The device can be developed into a portable, low-cost, point-of-care device leveraging the capabilities of the CMOS imagers to be pervasive in mobile electronics.

Introduction

There has been a major push of mobile technologies for personalized healthcare.[1–5] CMOS imagers that are present in almost all mobile devices have great potential for such applications because cell and tissue imaging reveals significant health and disease information.[6–16] It has been envisioned to make cytometers in a mobile device since a cytometer, being flow-based or image-based, can analyze the types, life cycles and phenotypical characteristics of cells.[17–21] There exist major challenges to reduce cytometers to be parts of mobile devices such as cellphones, concerning the physical construction of the devices and their operation in point-of-care and home settings. Cell analyzers in mobile devices can afford neither the sophisticated fluid control devices, lasers, photomultiplier tube (PMT) detectors and optics required by flow cytometers, nor the high-power microscope and the associated light sources and detection devices for image-based cytometers. For device operation, most users will not have the knowledge and skills and the auxiliary devices to stain or label the samples. On the other hand, the current label-free technique based on small and large angle light scatterings alone produces limited information. Those scattering signals are often used as the secondary signals with the primary fluorescent signals for cell-based assays.[22,23] Although the large angle (side scattering) signal is claimed to reveal the characteristics of the inner structure of a cell, the information is too coarse to give reliable and quantitative health information. Furthermore, without staining, the images from image-based cytometers lack the contrast for pathology and histology analyses. The above imposes a significant bottleneck in producing a viable cytometer using the CMOS imager in mobile devices. In this paper we report an innovative approach that addresses the above challenges to produce a high-quality cytometer fully compatible with mobile devices.

Realizing that the detailed nuclear structure of a cell carries more significant information than the overall size and shape of the cell itself,[24–30] we capture the key features of the cell nucleus by producing a ‘scattering profile’ of the nucleus that contains key features such as the nucleus volume, shape, morphology, *etc.* To put the nucleus features in the context of each cell, we use the same CMOS imager to capture the overall cell structure in a bright-field image. To overcome the orders of magnitude intensity difference well beyond the dynamic range of any CMOS imager, we have developed techniques to control the intensity and contrast of both the

---

[a] *Materials Science Program, University of California at San Diego, La Jolla, California 92093-0418, USA. E-mail: tfwu@jacobs.ucsd.edu; Fax: +1 8585342486; Tel: +1 8588222777*

[b] *Department of Bioengineering, University of California at San Diego, La Jolla, California 92093-0412, USA*

[c] *Department of Electrical and Computer Engineering, University of California at San Diego, La Jolla, California 92093-0407, USA*

[d] *Department of Chemistry and Biochemistry and San Diego Center for Systems Biology, University of California at San Diego, La Jolla, California 92093, USA*

† Electronic supplementary information (ESI) available. See DOI: 10.1039/c4lc00257a

bright-field image and the dark-field scattering image that are recorded in two regimes of the same CMOS sensor. The dark-field large-angle scattering image of the cell nucleus was obtained using an integrated micro cylindrical lens with a slit to produce an equivalent of light-sheet that slices through the moving cell. The bright-field image was produced by the autofluorescence of the microlens material excited by the UV component of a white LED lamp while blocking the primary beam from reaching the CMOS imager. The overall device is extremely simple to construct and operate, consisting of an LED lamp, an array of cylindrical microlenses with patterned slits, a low-cost magnification lens and an aperture in front of a commodity CMOS camera found in mobile devices.

After passing through the microlens (μlens) and a narrow slit, the LED light forms a light-sheet beam of 3 to 4 μm wide scanning through the samples on a moving glass slide. The light-sheet beam travelling through the cell cannot reach the CMOS sensor, and only the small fraction of light scattered by the cell nucleus at a specific angle can reach the CMOS sensor and form the dark-field scattering image of the portion of the cell being illuminated by the light-sheet. After the entire cell crosses the light-sheet, the scattering image of the full cell is recorded. Because the large angle scattering is dominated by Mie scattering governed by the contrast of the refractive index and the size of the object, the cell nucleus contributes most to the scattering image because of the high protein density within the nucleus of mammalian cells.[31,32] From the dark-field scattering patterns of the light-sheet beam, we were able to extract nuclear signatures as markers for cell classification and reconstruct the key features of the nucleus with high contrast and spatial resolution. We further created the bright-field image of the same cell after a preset time delay in a location that is at some distance from the dark-field scattering image. The acquisition of the bright field image that delineates the cell boundary following the dark-field nucleus image allows for the real-time verification of the dark-field scattering (whether from the cell nucleus or from the debris or dust particles) and correlates the cell nucleus with the cell body.

Since the cell nucleus structure changes throughout the cell cycle[33] and the cell cycle plays an important role in cell biology and clinics,[34,35] we have applied the compact, cellphone compatible cytometer device to observe the evolution of the nuclear structures during the cell cycle. For point-of-care applications, we have also used the device to interrogate human white blood cells and we have unequivocally shown different nuclear signatures for granulocytes and agranulocytes. In a straightforward process, the cell containing sample was smeared on a glass slide covered by a layer of liquid. The sample preparation protocol can be easily followed by any users without medical training. Among a wide variety of microfluidic devices designed for cell classification,[13,36,37] our device is the first and only device capable of revealing the sub-cellular structures in such great detail without labelling, in a design fully compatible with portable mobile devices from a device hardware and operation point of view.

Results

The working principal of a scattering-imaging-based cytometer and the characterization of the light-sheet beam formed by a μlens.

Fig. 1 shows the device design and principle for the detection of scattering images of cells. This compact cytometer has the samples sandwiched by two pieces of 150 μm thick glass coverslips (refractive index, $n \cong 1.45$). The top coverslip is patterned with an array of microcylindrical lenses and 10 μm slits formed by a 300 nm thick silver film. Each microcylindrical lens is 43 μm high at the apex, 160 μm wide and 2 mm long (Fig. S1†). The edge of the silver slit is 5 μm from the edge of the μlens. The bottom glass coverslip has a 15 μm high SU-8 wall as a reservoir to contain the fluid that immerses the cells immobilized on the glass slide. An LED or a filtered halogen lamp was used as the light source to minimize the speckle noise. The 10 μm slit underneath the microlens limits the portion of the lens to form the light-sheet, thus minimizing the effects of aberration and producing a good quality scattering image. The cell laden bottom glass coverslip is slid through the light-sheet beam by a stepping motor at a speed of $4.16\ \mu\text{m s}^{-1}$. A spatial filter is placed in front of the CMOS imager to block the primary transmitted beam, which would saturate the CMOS imager otherwise. As a result, only the scattered light of a scattering angle "Θ" between the light-sheet beam and the optical axis can pass through the focusing lens and the spatial filter to form an amplified image on the CMOS sensor. In a highly paralleled

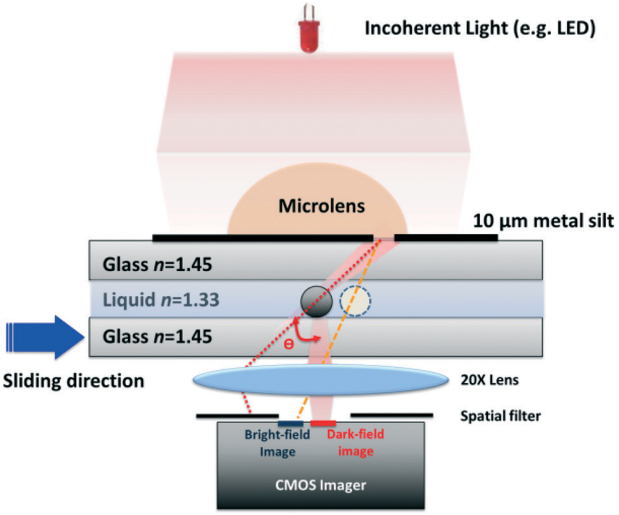

Fig. 1 The design of the scattering-imaging-based cytometer. Incoherent light is used to form a light-sheet beam by the microlens and the slit to scan through the cells. The autofluorescence of the lens material is used to form a transmitted bright-field image and the light-sheet beam is used to form the dark-field scattering image. The two images occur at different locations of the CMOS imager and can be overlaid to produce the complete cell image. Autofluorescent light by the lens material is used as the light source for the bright-field image so that the two images are of a similar intensity within the dynamic range of the CMOS sensor.

fashion, all cells on the glass coverslip can be scanned and recorded at a frame rate of 10 frames per second (fps) supported by off-the-shelf CMOS imagers.

The fabrication technique and characteristics of the μlens have been extensively studied.[38,39] We chose the back focal length of the μlens to be 183 μm, calculated from the equation

$$f_\mathrm{b} = n_2 \frac{n_1 R - (n_1 - 1)h}{n_1 (n_1 - 1)}$$

with the refractive indices of the μlens and glass being n_1 = 1.63 and n_2 = 1.45. The radius of the curvature can be calculated by $R = \frac{(d^2 + 4h^2)}{8h}$, where d and h are the diameter and height of the μlens, respectively. The numerical aperture (N.A.) of the μlens can be calculated by the formula: $\mathrm{N.A.} = n_2 \left\{ \frac{n_2{}^2}{n_1{}^2} \frac{4R\left[Rn_1 - (n_1 - 1)h\right]}{(n_1 - 1)^2 d^2} + 1 \right\}^{-\frac{1}{2}}$ to be 0.66.

To characterize the profile of the light-sheet-like beam, the scattering patterns of the 15 μm polystyrene beads were measured. As shown in Fig. 2(a), a dim spot appeared on the CMOS screen when the leading edge of the bead was intercepted by the light-sheet beam. The intensity of the scattered light increased when the light-sheet intersected a greater area of the bead and finally disappeared when the trailing edge of the bead passed the light-sheet. By converting the duration of the scattered light into the distance at a given travel speed of 4.16 μm s^{-1}, we obtained the intensity profile of the scattered light (Fig. S2†). A similar experiment was also performed with 7.66 μm diameter polystyrene beads to confirm the results. The intensity of the scattered light by the 7.66 μm beads was found to be 25% of that obtained when using 15 μm beads, showing that the light-sheet beam had a scattering intensity that was proportional to the cross-section or radius square of the bead. The time-lapse montage of bead scattering images enables us to find the width of the light-sheet beam. Fig. 2(b) shows the digitized scattering intensity over frames separated by 0.1 s or 0.416 μm. From Fig. 2(b) we determined the width of the light-sheet beam to be 3–4 μm. Fig. 2(c) shows a snapshot of a recorded video. Next to the scattering spots over the dark background is a bright band resulting from the autofluorescence of the μlens material under excitation of the blue/UV component of the light source. The intensity of the autofluorescent light can be tailored to the same order of magnitude as the scattering light so that both images are displayed simultaneously at different locations of the CMOS imager within its dynamic range. This unique feature provides a real-time verification of the detected images against contaminants such as cell debris and dust particles. In Fig. 2(c), polystyrene beads produce strong scatterings due to their large index contrast so a minimum amount of light is transmitted through, yielding dark images over the bright background. For biological cells having a weak index contrast with the liquid ambient, most of the autofluorescent light transmits through the cells and delineates the cell contours, which will be discussed later. A notable feature of the design that detects the scattered light in the dark field is the excellent signal-to-noise ratio of the images, which enables the extraction of fine features of the cell nucleus in high fidelity.

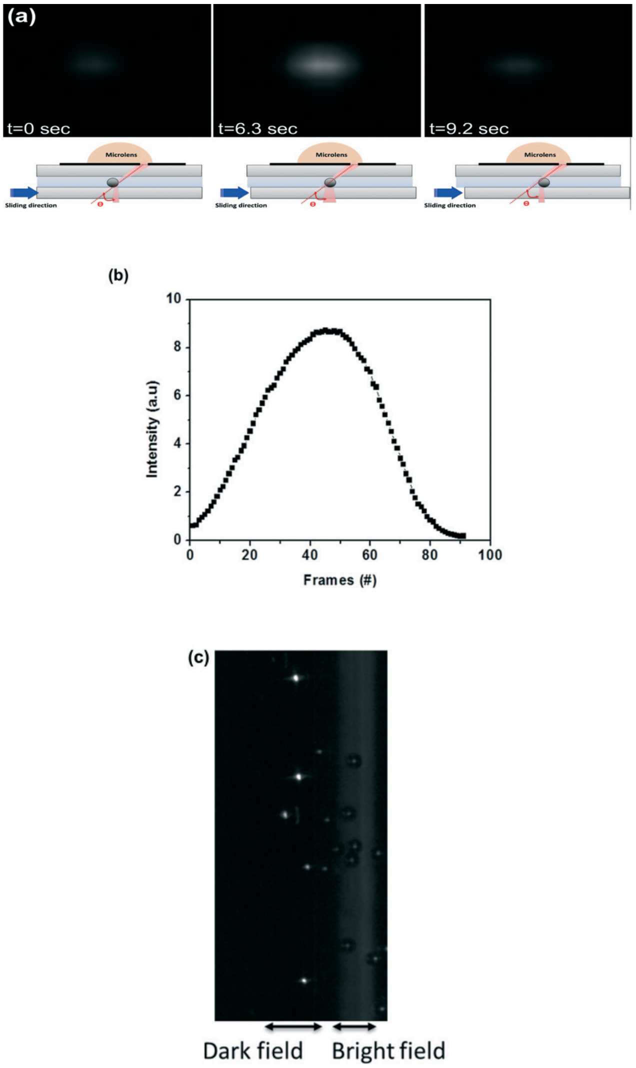

Fig. 2 (a) Snapshots of a 15 μm bead traveling the sensing area at different times. Θ, shown in the schematics, is the scattering angle between the optics axis and the transmitted light-sheet beam. (b) The intensity plot of the large angle scattering by a 15 μm bead (each frame represents a physical distance of 0.416 μm in this case). (c) A snapshot of 15 μm polystyrene beads interrogated with the scattering-imaging-based cytometer platform, showing the dark-field scattering images and the bright-field image right next.

The observation of HEK293 cell cycles and the construction of nuclear signatures

Because the nucleus of the mammalian cells is the dominant object responsible for light scattering, the dark-field images of the CMOS imager reveal the unique properties of the cell nuclei as effective markers for applications such as disease diagnosis, cell classification, and cell cycle monitoring. To demonstrate the feasibility of the scattering-imaging-based cytometer for label-free cell nucleus detection, we used cultured HEK293 cell lines where cells had uniform properties but went through different life cycles (see Methods). By smearing 5 μL of a HEK293 cell suspension in PBS on a poly-D-lysine treated glass coverslip, various HEK293 cells were observed in Fig. 3(a). The dark-field images from the nucleus scattering and the contour of the same cell in the bright-field image were displayed in two separate regions of the CMOS imager at a time delay of 9.8 ± 0.2 seconds when the cell on the sample slide travelled from the scattering detection region to the whole cell imaging region. Superimposing the two time-lagged images allows us to construct the full-cell image with its nucleus in the right position of the cell body. Fig. 3(b) shows the occasion when the cell was in the mitotic phase where the new cell membrane separating the individual cells was in formation. Notably in such a case the dark-field scattering image showed two bright spots from two nuclei and the bright-field image showed the membrane of the cells being still connected. These results demonstrate that whether the cells exist in a discrete, adjacent, overlapped or dividing form, they can be distinguished by our device by combining the dark-field and bright-field images from a single CMOS imager. To more specifically monitor cells in different cycles, we cultured HEK293 cells with inhibitors to stop the cells at different checkpoints. Mitomycin was used to arrest the cell cycle at the G1 phase,[40] where the biosynthetic activities of cells were activated to form necessary proteins for the next phase (S phase) and thus the size of cells slightly increased. Fig. 3(c) shows the images of a single HEK293 cell passing through the dark-field and bright-field, respectively. Similar to uncontrolled HEK293 cells, the scattering image by the cell nucleus was visible in the dark field, followed by the bright-field image. Separately, nocodazole was used to arrest the HEK293 cells at the G2/M phase, more specifically at the prometaphase (Fig. S3†). After undergoing the G2 phase, cells become even larger, but without microtubule attachment cells cannot proceed beyond the prometaphase. When arrested at the prometaphase, the nuclear membrane breaks down and the constituents of the nucleus are distributed within the cytoplasm. Lacking a well-defined nucleus confined by the nucleus membrane, the cell has no dominant scattering center. As a result, the scattering images were barely seen in the dark-field even with an increased exposure time by 300%, as shown in Fig. 3(d).

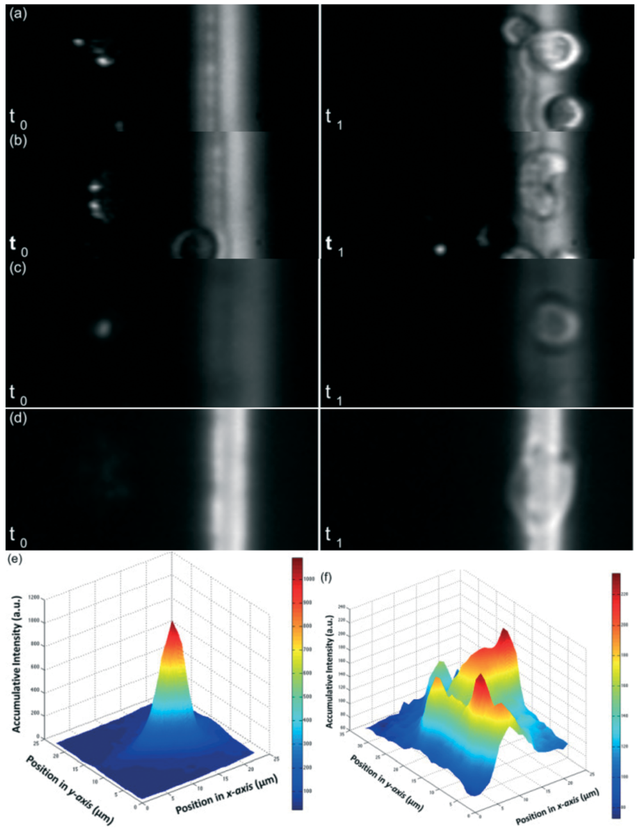

Fig. 3 (a) and (b) Snapshots of uncontrolled HEK293 cells taken by a CMOS imager, where HEK293 cells were first imaged for the scattering patterns in the dark field, and then imaged in the bright field to delineate the cell boundaries. (c) and (d) Snapshots of HEK293 cells arrested at the G1/S phase and the prometaphase stage, respectively. The time lapse between t_0 and t_1 is 9.8 ± 0.2 s for (a) to (d). The exposure time in (d) is 3 times as long as (c) to underline the large difference in the nucleus scattering intensity for cells in two different phases. (e) and (f) The 3-dimensional contour plots of the nuclei of the HEK293 cells arrested at the G1/S stage and at prometaphase stage.

It is further shown that the diameter of the cells smeared on the glass coverslip can be estimated from the bright field images, to be 21.78 ± 2.47 μm and 31.79 ± 3.45 μm for cells at the G1/S (n = 10) stage and the prometaphase (n = 10), respectively. From the dark-field and bright-field images of the same cell, we reconstruct the features of the cell nucleus within the cell boundary. Fig. 3(e) and (f) show the 3-dimensional contour plots of the nuclei of the HEK293 cells at the G1 and prometaphase stages, respectively. As shown in Fig. 3(e), the size of the nucleus at the G1 phase is averaged to be about 16 μm; however, the size of the nucleus at the prometaphase cannot be estimated due to the lack of a definable nuclear shape.

The differentiation of white blood cells with nuclear signatures

Although most types of mammalian cells have round or oval shape nuclei, the distinct nuclear shapes in the white blood cell family stand out particularly and attract significant attention clinically. Different types of white blood cells (WBCs) play important and distinct roles in the immune system, and the nuclear shapes of the WBCs can be used as effective markers for WBC classification. From the nuclear morphologies, WBCs can be categorized into mononuclear (MN) and polymorphonuclear (PMN) cells. MN WBCs such as lymphocytes and monocytes have a single nucleus. In contrast, PMN WBCs such as neutrophils have 2–5 lobes in their nucleus. To investigate the cell differentiation capability of the device, we isolate PMN WBCs from MN WBCs from whole blood using the Hypaque–Ficoll method[41] (see Methods), which produces

PMN and MN WBC samples with >90% purity in each sample (Fig. S4†). The experiments were performed separately with these PMN and MN WBC samples on poly-D-lysine treated glass coverslips. Fig. 4(a) and (b) show the snapshots of the MN and PMN WBCs on the sliding coverslips. The dark-field scattering images of the PMN cells appear to be brighter than the MN cells and display spotty patterns, signifying the polymorphonuclear features of the cells. The bright-field image shows the diameters of the MN ($n = 10$) and PMN ($n = 10$) cells to be 10.12 ± 1.01 μm and 12.54 ± 1.39 μm, respectively. Fig. 4(c) and (d) exemplify the 2-dimensional and 3-dimensional contour plots of an MN cell, showing clearly the characteristics of a single lobe nucleus. In contrast, the 2-dimensional and 3-dimensional contour plots of a PMN cell, as shown in Fig. 4(e) and (f), show two main peaks and a satellite peak near one of the main peaks as the multi-lobed nucleus characteristics of neutrophils. Unlike the MN nucleus that shows a uniform nucleus contour within the cell body, the nucleus images of the PMN cells vary significantly and in many cases show four lobes (Fig. S5†). The variability is attributed to the orientation of the cell nucleus with respect to the incident light-sheet beam. For example, the light scattering from an oval shaped nucleus may generate a smaller but brighter image or a larger but dimmer image depending on the relative orientation between the nucleus and the light-sheet beam. However, independent of the orientation of the nucleus, the total intensity of the nucleus summed over all the pixels is proportional to the volume of the nucleus, which is less invariant for a given cell type. Fig. 4(g) shows the integrated scattering intensity of the PMN cells and MN cells and the results indicate that the nucleus volume of the PMN cells are nearly 3 times as large as the nucleus volume of the MN cells.

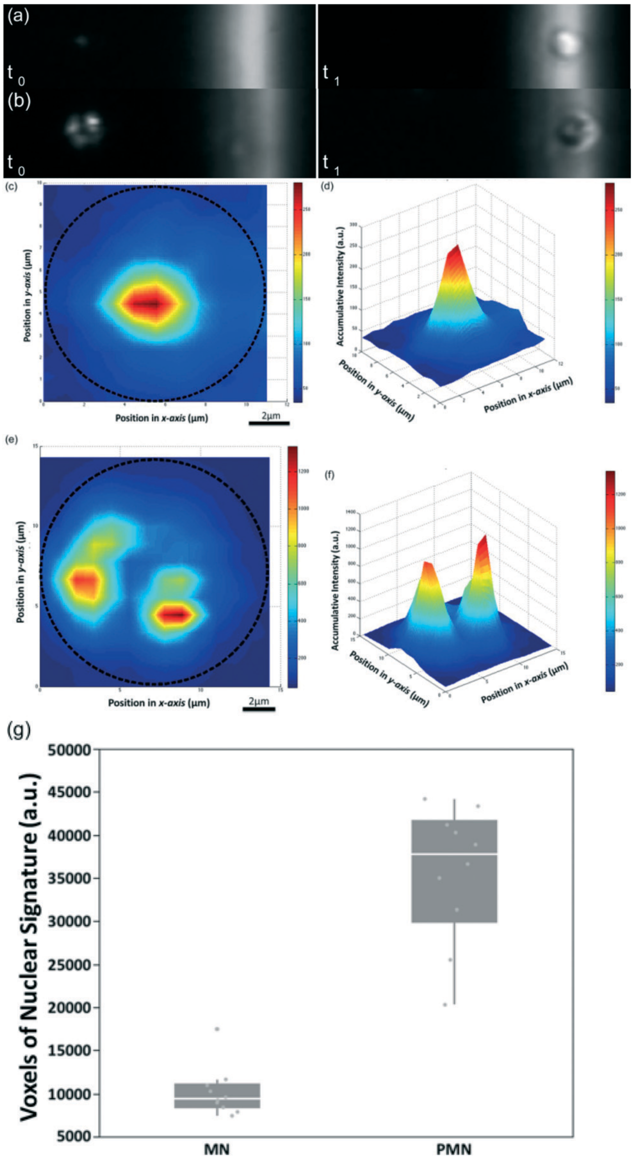

Fig. 4 (a) Snapshots of mononuclear cells, *e.g.* lymphocytes and (b) snapshots of polymorphonuclear cells, *e.g.* neutrophils. All cells travelled through the dark-field imaging area first and then the bright-field imaging area. (c) and (d) are the 2-dimensional and 3-dimensional contour plots of a mononuclear cell, respectively. (e) and (f) are the 2-dimensional and 3-dimensional contour plots of a polymorphonuclear cell, respectively. (g) A box chart of voxels under the 3-dimensional contour plot for mononuclear and polymorphonuclear cells, indicating the accumulative voxels, being proportional to the total volume of the nucleus, have a relatively tight distribution for each cell type.

Discussion

We have demonstrated a scattering-imaging-based cytometer for biosensing with a simple design that is compatible with mobile devices. The design leverages from the commodity CMOS sensors found ubiquitously in consumer electronics. Utilizing the light-sheet beam produced by a light emitting diode and a microcylindrical lens on a slit, the device can reveal two complementary cell images in two well defined locations of the CMOS sensor: a dark-field image due to light scattering primarily by the nucleus and a bright-field image from the autofluorescent light of the lens material transmitting through the cell body. In an extremely simple, label-free sample preparation process to form a cell/tissue smear on a glass slide, the features of the nucleus and the overall cell shape are imaged separately with precise spatial relations between them. By overlaying the two images digitally, we obtain entire cell images with sufficient details and resolution for biological and clinical utilities. The device is expected to have significant values in point-of-care applications, especially in areas lacking medical infrastructures.

All the experimental results reported in this work are cells smeared on a coverslip and immersed in a thin (15 μm) layer of fluid. For convenience of operation, we have mechanically coupled the slide to a syringe pump and used the motor of the syringe pump to push the slides across the light-sheet beam. However, we should point out that the operation of the device does not require a syringe pump since no flow injection is required. Furthermore, the requirement for the control of the motor speed is also very relaxed and the operation has high tolerances to motion jitters. With the registration markers on the glass slide, similar to our earlier work on the space-time coding method,[36,42,43] the CMOS camera imager can also work as a motion detector to obtain the instantaneous travel speed of the slide by tracking the lithographically defined markers on the slide.

In our design the lateral field of view of the CMOS imager is 460 μm for each micro cylindrical lens. At a scanning speed of 4.16 μm per second, the device can scan through 10 mm^2 in 20 minutes with a 1 × 4 microlens array. The throughput can be increased with an increasing travel speed to the extent that the travel does not cause shear stress to disturb the cells immobilized on the glass slide. The width of the light-sheet in the current system is 3–4 μm across the 15 μm spacing where cells are located. The achievable spatial resolution from the system is estimated to be around 1 μm by deconvolution of the images from the beam profile through signal processing. The current design produces a 20× magnified image on the CMOS sensor, so the pixel size of the CMOS sensor does not limit the resolution. Ultimately the image quality and resolution is limited by the noise of the CMOS sensor and the quality of the microlens. Although the microlens can produce significant aberration, its influence in the image quality is reduced by the 10 μm slit underneath. Since only a small portion of the lens is utilized to form the light-sheet beam, optical aberration can be greatly reduced, making it possible to demonstrate a high quality image in such a simple and compact system.

To prove that the cell nucleus contributes to the scattering image, images were taken from HEK293 cells arrested at the prometaphase stage where the nuclear membrane disintegrates. The results show that, without a well-defined nucleus, the scattering intensity drops to a level that is hardly detectable. As a result, the device can clearly detect and identify cell cycles. Experiments were also conducted to demonstrate the utility of acquisition of the dark-field scattering image and bright-field transmitted cell image by a single CMOS imager. This attractive capability is attributed to several unique designs, including utilizing the autofluorescence of the lens material to attenuate the light intensity to a level comparable to the large angle scattering light without saturating the CMOS sensor. The availability of the dark-field and bright-field images that are present side by side provides effective means for the real-time verification to remove artifacts from cell debris or dust particles. It also allows for the accurate construction of the full cell image showing the cell nucleus within the cell body. The experiments with white blood cells demonstrate unequivocal distinction between the PMN white blood cells (*e.g.* neutrophils) and the MN white blood cells (*e.g.* lymphocytes). The device provides a promising solution for one of the most critical point-of-care challenges, namely label-free cell classification. Without fluorescent labelling or staining, even a commercial flow cytometer or imaging cytometer cannot produce reliable results to classify cells, due to the noisy and widely spread side scattering signals resulting from the inhomogeneity of cells. Our device offers extra dimensions of information about the nuclear granularity beyond the side scattering intensity measured by flow cytometers, and the spatially distributed scattering plots reveal not only the inhomogeneity of the cells of the same cell type but also the commonality of them, exemplified by the same cell type undergoing different life cycles and subpopulations of white blood cells.

Experimental methods

The fabrication of scattering-imaging-based cytometer platform

The thermally reflowed photoresist that was photographically patterned on the glass substrate was used to generate the microlens (μlens). The pattern of the μlens was designed to be a 2200 μm × 160 μm (length × width) rectangle on the transparent photo-mask (CAD/Art services, Inc.). To obtain the light-sheet-like beam, a silver film with an opening of 2000 μm × 10 μm (length × width) was deposited on the thin glass (~150 μm in thickness) by a conventional metal lift-off process. To obtain the desired microlens shape, a double resist spinning process was employed. A SPR220-7.0 (Shipley) photoresist was first coated at 1200 rpm for 40 seconds and baked at 80 °C for 1 minute. The second SPR220-7.0 spin-coating process was performed at 1200 rpm for 40 seconds. Prior to the UV exposure with the Karl Suss MA6 mask aligner, the double-coated sample was stored for at least one day in the ambient environment. The alignment between the layer of the μlens and the Ag slits was conducted carefully to keep a 5 μm space between the edge of the microcylindrical lens and the edge of the slit. After the exposure process, the photoresist from all areas but the microlens areas was removed by resist development. The photoresist over the microlens area was heated to 140 °C for 1 hour at a ramping rate of 25 °C per hour on the hot plate. After the reflow of the melt photoresist, the μlens had a half-dome shape with a 160 μm base width and a 43 μm height, characterized by Dektak 150 surface profiler (Fig. S1†). To form the reservoir to contain the fluid that covers the cells on the slide, a negative photoresist, SU8-2050, was spun on a glass substrate to form a 3 cm × 1.5 cm × 15 μm (length × width × height) rectangular chamber with a rim thickness of 500 μm.

Experimental setup

To characterize the scattering-imaging-based cytometer, we prepared samples with cancer cells (HEK293 cells) and isolated WBCs (the procedure is discussed later). HEK293 (Human Embryonic Kidney) cells were cultured in Dulbecco's Modified Eagle Medium (DMEM) supplemented with 10% (v/v) fetal bovine serum (FBS) and 1% (v/v) penicillin/streptomycin (PS) in a humidified incubator at 37 °C in 5% CO_2. The whole blood samples used to produce the mononuclear and polymorphonuclear WBC samples were purchased from the blood bank (San Diego Blood Bank). All cell samples were suspended in a phosphate buffered saline (PBS) solution prior to the experiment. The poly-D-lysine (Sigma P-0899) solution was prepared to have a concentration of 0.2 mg mL^{-1} and applied to the glass coverslip with the cell reservoir.

The glass coverslip was incubated at room temperature for 1 hour and then rinsed 3 times with PBS. 5 μL of the cell sample was pipetted onto the pretreated glass coverslip. The μlens-covered glass coverslip was used to spread the sample over the glass coverslip at a smearing angle of about 10 degrees. As illustrated in Fig. 1, the samples sandwiched between the two glass coverslips were placed on the stage and the bottom slip that the cells resides on was mechanically coupled to the stepping motor of a syringe pump to slide the glass slip at a speed of 4.16 μm s^{-1}. A white LED or a filtered halogen lamp was used to illuminate the glass coverslips through the microlens. A 20× lens (N.A. 0.45) was placed between the cell sample and the CMOS imager and the images were recorded by a CMOS imager at 10 frames per second.

HEK293 cell cycle control

In the experiment to arrest the HEK293 cells at the G1 phase, Mitomycin (10 μg ml^{-1}) dissolved in DMEM, mixed with 0.5% (v/v) FBS and 1% (v/v) PS, was added to the culture medium and then cells were incubated for 3 hours prior to the experiment. To stop the cell cycle at the G2/M stage, 50 ng ml^{-1} of nocodazole in DMEM was mixed with 0.5% (v/v) FBS and 1% PS and the cells were cultured for 16 hours. A commercial flow cytometer was used to analyze the cell samples afterwards to confirm the effectiveness of the cell cycle control. Cells at the designed stages were washed with PBS and suspended in ice-cold 70% ethanol. After keeping the cell suspension at 4 °C for 30 minutes, the sample was centrifuged at 2000 rpm for 5 minutes and the supernatant of the cell suspension was carefully discarded. After washing the sample left in the tube with PBS twice, the fixed cells were resuspended in 500 μL PBS and 2.5 μL RNAse (Invitrogen 12091-021) was added to the cell suspension. After a 15 minute incubation at room temperature and another centrifuge and supernatant removal step, 25 μL propidium iodide (PI) was added to the cell suspension in 500 μL PBS. The cells were incubated for 5 minutes at room temperature and rinsed by PBS and the sample was ready for analysis by commercial flow cytometers. We analyzed these stained cells by an Accuri C6 flow cytometer to collect at least 20 000 events per sample (Fig. S3†).

The isolation of PMN and MN cells from human whole blood

The Hypaque–Ficoll method described in ref. 41 with some modifications was used to isolate specific white blood cells from whole blood. 6 mL of whole blood purchased from the blood bank was mixed with red blood cell lysis buffer (eBioscience, CA) and kept at room temperature for 10 minutes. After centrifugation at 1600 rpm for 5 minutes, the cell pellets were rinsed with a buffer solution consisting of 10 mM ethylenediaminetetraacetic acid (EDTA) and 1X PBS, which was followed by another centrifugation. The cells were carefully resuspended in 2.5 mL of PBS. The cell suspension was layered over 3 mL of Hypaque–Ficoll solution (Sigma 1077) in a 15 mL canonical tube and spun at 1500 rpm for 45 minutes at 4 °C using a low brake. To obtain MN cells, we carefully extracted the layer of cells between the top level solution and the Hypaque–Ficoll solution. To obtain the PMN cells, the bottom cell pellet was taken out. Both types of cells were suspended in a Ca^{2+} and Mg^{2+}-free Hank's balanced salt solution (Sigma) for further experiments.

Conclusion

In conclusion, using a simple device compatible with mobile consumer devices such as iphones and ipads, we have presented a label-free cell analyzer capable of detecting the inner structures of cells. The device has the potential to satisfy the unmet needs for point-of-care applications in areas lacking medical infrastructures.

Acknowledgements

We thank Mr Kuen-Han Lin for suggestions on the algorithms of imaging processing. We also thank Dr Ian Lian and Dr Ti-Hsuan Ku for providing cell culture support to conduct preliminary experiments.

References

1 D. N. Breslauer, R. N. Maamari, N. A. Switz, W. A. Lam and D. A. Fletcher, *PLoS One*, 2009, **4**, e6320.

2 F. B. Myers and L. P. Lee, *Lab Chip*, 2008, **8**, 2015.

3 A. W. Martinez, S. T. Phillips, E. Carrilho, S. W. Thomas, H. Sindi and G. M. Whitesides, *Anal. Chem.*, 2008, **80**, 3699.

4 M. Zimic, J. Coronel, R. H. Gilman, C. G. Luna, W. H. Curioso and D. A. J. Moore, *Trans. R. Soc. Trop. Med. Hyg.*, 2009, **103**, 638.

5 P. Yager, G. J. Domingo and J. Gerdes, *Annu. Rev. Biomed. Eng.*, 2008, **10**, 107.

6 Q. Wei, R. Nagi, K. Sadeghi, S. Feng, E. Yan, S. J. Ki, R. Caire, D. Tseng and A. Ozcan, *ACS Nano*, 2014, **8**, 1121–1129.

7 G. A. Zheng, S. A. Lee, Y. Antebi, M. B. Elowitz and C. H. Yang, *Proc. Natl. Acad. Sci. U. S. A.*, 2011, **108**, 16889.

8 H. Y. Zhu, S. O. Isikman, O. Mudanyali, A. Greenbaum and A. Ozcan, *Lab Chip*, 2013, **13**, 51.

9 D. Gallegos, K. D. Long, H. J. Yu, P. P. Clark, Y. X. Lin, S. George, P. Nath and B. T. Cunningham, *Lab Chip*, 2013, **13**, 2124.

10 H. Y. Zhu, S. Mavandadi, A. F. Coskun, O. Yaglidere and A. Ozcan, *Anal. Chem.*, 2011, **83**, 6641.

11 A. F. Coskun, J. Wong, D. Khodadadi, R. Nagi, A. Tey and A. Ozcan, *Lab Chip*, 2013, **13**, 636.

12 O. Mudanyali, S. Dimitrov, U. Sikora, S. Padmanabhan, I. Navruz and A. Ozcan, *Lab Chip*, 2012, **12**, 2678.

13 H. Y. Zhu, I. Sencan, J. Wong, S. Dimitrov, D. Tseng, K. Nagashima and A. Ozcan, *Lab Chip*, 2013, **13**, 1282.

14 I. Navruz, A. F. Coskun, J. Wong, S. Mohammad, D. Tseng, R. Nagi, S. Phillips and A. Ozcan, *Lab Chip*, 2013, **13**, 4015.

15 X. Q. Cui, L. M. Lee, X. Heng, W. W. Zhong, P. W. Sternberg, D. Psaltis and C. H. Yang, *Proc. Natl. Acad. Sci. U. S. A.*, 2008, **105**, 10670.

16 Q. S. Wei, H. F. Qi, W. Luo, D. Tseng, S. J. Ki, Z. Wan, Z. Gorocs, L. A. Bentolila, T. T. Wu, R. Sun and A. Ozcan, *ACS Nano*, 2013, **7**, 9147.

17 H. J. Yoo, J. Park and T. H. Yoon, *Cytometry, Part A*, 2013, **83A**, 356.

18 D. R. Albrecht, G. H. Underhill, J. Resnikoff, A. Mendelson, S. N. Bhatia and J. V. Shah, *Integr. Biol.*, 2010, **2**, 278.

19 E. Schonbrun, S. S. Gorthi and D. Schaak, *Lab Chip*, 2012, **12**, 268.

20 M. J. Kim, K. H. Lim, H. J. Yoo, S. W. Rhee and T. H. Yoon, *Lab Chip*, 2010, **10**, 415.

21 K. H. Lim, J. Park, S. W. Rhee and T. H. Yoon, *Cytometry, Part A*, 2012, **81A**, 691.

22 S. H. Cho, J. Godin, C. H. Chen, W. Qiao, H. Lee and Y. H. Lo, *Biomicrofluidics*, 2010, **4**, 043001.

23 E. J. van der Vlist, E. N. M. Nolte-'t Hoen, W. Stoorvogel, G. J. A. Arkesteijn and M. H. M. Wauben, *Nat. Protoc.*, 2012, **7**, 1311.

24 M. Versaevel, M. Riaz, T. Grevesse and S. Gabriele, *Soft Matter*, 2013, **9**, 6665.

25 M. Versaevel, T. Grevesse and S. Gabriele, *Nat. Commun.*, 2012, **3**, 671.

26 M. Webster, K. L. Witkin and O. Cohen-Fix, *J. Cell Sci.*, 2009, **122**, 1477.

27 Y. Fu, L. K. Chin, T. Bourouina, A. Q. Liu and A. M. J. VanDongen, *Lab Chip*, 2012, **12**, 3774.

28 K. H. Chow, R. E. Factor and K. S. Ullman, *Nat. Rev. Cancer*, 2012, **12**, 196.

29 D. Zink, A. H. Fischer and J. A. Nickerson, *Nat. Rev. Cancer*, 2004, **4**, 677.

30 H. Lans and J. H. J. Hoeijmakers, *Nature*, 2006, **440**, 32.

31 R. Barer and S. Joseph, *Quart. J. Microscop. Sci.*, 1954, **95**, 399.

32 R. Barer and K. A. F. Ross, *J. Physiol.*, 1952, **118**, P38.

33 M. Hesse, *et al.*, *Nat. Commun.*, 2012, **3**, 1076.

34 M. Kawasaki, K. Sasaki, T. Satoh, A. Kurose, T. Kamada, T. Furuya, T. Murakami and T. Todoroki, *Cell Proliferation*, 1997, **30**, 139.

35 J. Y. Wang, P. P. Lou, R. Lesniewski and J. Henkin, *Anti-Cancer Drugs*, 2003, **14**, 13.

36 T. F. Wu, Z. Mei and Y. H. Lo, *Lab Chip*, 2012, **12**, 3791.

37 T.-F. Wu, Z. Mei and Y.-H. Lo, *Sens. Actuators, B*, 2013, **186**, 327.

38 J. Lim, P. Gruner, M. Konrad and J. C. Baret, *Lab Chip*, 2013, **13**, 1472.

39 J. Chen, W. S. Wang, J. Fang and K. Varahramyan, *J. Micromech. Microeng.*, 2004, **14**, 675.

40 S. G. Kang, H. Chung, Y. D. Yoo, J. G. Lee, Y. I. Choi and Y. S. Yu, *Curr. Eye Res.*, 2001, **22**, 174.

41 W. Nauseef, in *Neutrophil Methods and Protocols*, ed. M. Quinn, F. DeLeo and G. Bokoch, Humana Press, 2007, vol. 412, p. 15.

42 T. F. Wu, Z. Mei, L. Pion-Tonachini, C. Zhao, W. Qiao, A. Arianpour and Y. H. Lo, *AIP Adv.*, 2011, **1**, 022155.

43 Z. Mei, T. F. Wu, L. Pion-Tonachini, W. Qiao, C. Zhao, Z. W. Liu and Y. H. Lo, *Biomicrofluidics*, 2011, **5**, 034116.